

1 **A record of plume-induced plate rotation triggering seafloor spreading and**  
2 **subduction initiation**

3  
4 **Authors:** Douwe J.J. van Hinsbergen<sup>1\*</sup>, Bernhard Steinberger<sup>2,3</sup>, Carl Guilmette<sup>4</sup>, Marco  
5 Maffione<sup>1,5</sup>, Derya Gürer<sup>1,6</sup>, Kalijn Peters<sup>1</sup>, Alexis Plunder<sup>1,7</sup>, Peter J. McPhee<sup>1</sup>, Carmen Gaina<sup>3</sup>,  
6 Eldert L. Advokaat<sup>1,5</sup>, Reinoud L.M. Vissers<sup>1</sup>, and Wim Spakman<sup>1</sup>

7 **Affiliations:**

8 <sup>1</sup>Department of Earth Sciences, Utrecht University, Princetonlaan 8A, 3584 CB Utrecht,  
9 Netherlands

10 <sup>2</sup>GFZ German Research Centre for Geosciences, Potsdam, Germany

11 <sup>3</sup>Centre of Earth Evolution and Dynamics (CEED), University of Oslo, Norway

12 <sup>4</sup>Département de Géologie et de Génie Géologique, Université Laval, Québec, QC G1K 7P4,  
13 Canada

14 <sup>5</sup>School of Geography, Earth and Environmental Sciences, University of Birmingham, B15 2TT,  
15 UK

16 <sup>6</sup>School of Earth and Environmental Sciences, University of Queensland, St Lucia, Queensland  
17 4072, Australia

18 <sup>7</sup>BRGM, F-45060, Orléans, France

19  
20 \*Correspondence to: Douwe J.J. van Hinsbergen ([d.j.j.vanhinsbergen@uu.nl](mailto:d.j.j.vanhinsbergen@uu.nl))

21  
22 ***Manuscript under consideration at Nature Geoscience:***

23 *Original submission date: July 10, 2020*

24 *Reviews received: December 18, 2020*

25 *Resubmission after revision: January 26, 2020*

27 **The formation of a global network of plate boundaries surrounding a mosaic of**  
28 **lithospheric fragments was a key step in the emergence of Earth's plate tectonics. So far,**  
29 **propositions for plate boundary formation are regional in nature but how plate boundaries**  
30 **are being created over 1000s of km in short periods of geological time remains elusive.**  
31 **Here, we show from geological observations that a >12,000 km long plate boundary formed**  
32 **between the Indian and African plates around 105 Ma with subduction segments from the**  
33 **eastern Mediterranean region to a newly established India-Africa rotation pole in the west-**  
34 **Indian ocean where it transitioned into a ridge between India and Madagascar. We find no**  
35 **plate tectonics-related potential triggers of this plate rotation and identify coeval mantle**  
36 **plume rise below Madagascar-India as the only viable driver. For this, we provide a proof**  
37 **of concept by torque balance modeling revealing that the Indian and African cratonic keels**  
38 **were important in determining plate rotation and subduction initiation in response to the**  
39 **spreading plume head. Our results show that plumes may provide a non-plate-tectonic**  
40 **mechanism for large plate rotation initiating divergent and convergent plate boundaries**  
41 **far away from the plume head that may even be an underlying cause of the emergence of**  
42 **modern plate tectonics.**

43 The early establishment of plate tectonics on Earth was likely a gradual process that  
44 evolved as the cooling planet's lithosphere broke into a mosaic of major fragments, separated by  
45 a network of plate boundaries: seafloor spreading ridges, transform faults, and subduction  
46 zones<sup>1</sup>. The formation of spreading ridges and connecting transform faults is regarded as a  
47 passive process, occasionally associated with rising mantle plumes<sup>2</sup>. The formation of  
48 subduction zones is less well understood. Explanations for subduction initiation often infer  
49 spontaneous gravitational collapse of aging oceanic lithosphere<sup>2</sup>, or relocations of subduction  
50 zones due to intraplate stress changes in response to continental collisions with other continents,  
51 oceanic plateaus, or arcs<sup>3</sup>. Mantle plumes have also been suggested as drivers for regional  
52 subduction initiation, primarily based on numerical modeling<sup>4-6</sup>. But while such processes may  
53 explain how plate tectonics evolves on a regional scale, they do not provide insight into the  
54 geodynamic cause(s) for the geologically sudden (<10 My) creation of often long (>1000 km)  
55 plate boundaries including new subduction zones<sup>7</sup>. Demonstrating the causes of plate boundary  
56 formation involving subduction initiation using the geological record is challenging and requires  
57 (i) establishing whether subduction initiation was spontaneous or induced; (ii) if induced,

58 constraining the timing and direction of incipient plate convergence; (iii) reconstructing the  
59 entire plate boundary from triple junction to triple junction, as well as the boundaries of  
60 neighboring plates, to identify collisions, subduction terminations, or mantle plume arrival that  
61 may have caused stress changes driving subduction initiation. In this paper, we provide such an  
62 analysis for an intra-oceanic subduction zone that formed within the Neotethys ocean around 105  
63 Ma, to evaluate the driver of subduction initiation and plate boundary formation.

64

### 65 **Induced subduction initiation across the Neotethys Ocean**

66 Determining spontaneous versus induced subduction initiation is a particular complexity  
67 in this analysis and requires geological records of both the upper and lower plates: in both cases,  
68 subduction initiation corresponds with initial lower plate burial, whereas coeval or delayed  
69 extension in the upper plate are contrasting diagnostics of spontaneous or forced subduction  
70 initiation, respectively<sup>8</sup>. Initiation of lower plate burial can be dated through prograde mineral  
71 growth in rocks of the incipient subduction plate contact, in so-called metamorphic soles<sup>8</sup>. The  
72 timing of extension is inferred from spreading records in so-called supra-subduction zone (SSZ)  
73 ophiolites<sup>8-10,11</sup>. Such SSZ ophiolites have a chemical stratigraphy widely interpreted as having  
74 formed at spreading ridges above a nascent subduction zones. Metamorphic sole protoliths  
75 typically reveal that also the initial downgoing plate was of oceanic composition<sup>2,9</sup>, and so  
76 ophiolite belts with metamorphic soles demarcate fossil juvenile intra-oceanic subduction plate  
77 boundaries.

78 Several SSZ ophiolite belts exist in the Alpine-Himalayan mountain belt, which formed  
79 during the closure of the Neotethys Ocean<sup>12,13</sup> (Fig. 1A). One of these ophiolite belts formed in  
80 Cretaceous time and runs from the eastern Mediterranean region to Pakistan, across northern  
81 Arabia. The timing of lower plate burial as well as upper plate extension have been constrained  
82 in this ophiolite belt through detailed geochronological, petrological, and geochemical work.  
83 Incipient lower plate burial has been dated through Lu/Hf prograde garnet growth ages of ~104  
84 Ma in Oman as well as in the eastern Mediterranean region<sup>8,14</sup>. Upper plate extension and SSZ  
85 ophiolite spreading has been dated using magmatic zircon U/Pb ages and synchronous  
86 metamorphic sole <sup>40</sup>Ar/<sup>39</sup>Ar cooling ages and occurred at 96-95 Ma (Pakistan, Oman)<sup>15,16</sup> to 92-  
87 90 Ma (Iran, eastern Mediterranean region)<sup>17</sup>. The 8-14 Myr time delay between initial lower

88 plate burial and upper plate extension demonstrates that initiation of this subduction zone was  
89 not spontaneous, but induced by far-field forcing<sup>8</sup>.

90 An initial ~E-W convergence direction at this subduction zone was constrained through  
91 paleomagnetic analysis and detailed kinematic reconstruction of post-subduction initiation  
92 deformation of the eastern Mediterranean region, Oman, and Pakistan, and was accommodated at  
93 ~N-S striking trench segments<sup>13,18-20</sup>. This is surprising: for hundreds of Ma, throughout the  
94 Tethyan realm rifts and ridges formed breaking fragments off northern Gondwana in the south,  
95 which accreted at subduction zones to the southern Eurasian margin in the north<sup>21,22</sup>. The ~E-W  
96 convergence that triggered ~105 Ma subduction initiation across the Neotethys ocean was thus  
97 near orthogonal to the long-standing plate motions. To find this trigger we developed the first  
98 comprehensive reconstruction of the entire ~12,000 km long plate boundary that formed at ~105  
99 Ma and placed this in context of reconstructions of collisions and mantle plumes of the  
100 Neotethyan realm.

101

## 102 **Geological reconstruction of plate boundary formation across the Neotethys**

103 The Cretaceous SSZ ophiolites that formed at the Cretaceous intra-Neotethyan  
104 subduction zone in its juvenile stages are now found as klippen on intensely deformed orogenic  
105 belts (Fig. 1A). These belts formed during subduction zone migration and collisions with the  
106 continents of Greater Adria, Arabia, and India. We reconstructed these orogenic belts (Fig. 1)  
107 and restored the Cretaceous ophiolites into their original configuration (Fig. 1C) (see Methods).

108 The westernmost geological record of the Cretaceous intra-Neotethyan subduction zone  
109 is found in eastern Greece and western Turkey, where it ended in a trench-trench-trench triple  
110 junction with subduction zones along the southern Eurasian margin<sup>18</sup>. From there, east-dipping  
111 (in the west) and west-dipping (in the east) subduction segments followed the saw-toothed shape  
112 of the Greater Adriatic and Arabian continental margins (Fig. 1C) and initiated close to it: rocks  
113 of these margins already underthrust the ophiolites within 5-15 My after SSZ ophiolite  
114 spreading<sup>14,23,24</sup>, and continent-derived zircons have been found in metamorphic sole rocks<sup>25</sup>.  
115 Subduction segments that likely nucleated along ancient N-S and NE-SW trending fracture  
116 zones, linked through highly oblique, north-dipping subduction zones that trended parallel to and  
117 likely reactivated the pre-existing (hyper)extended passive margins (Fig. 1B, C)<sup>20,23</sup>. Subducted

118 remnants of the Cretaceous intra-Neotethyan subduction are well-resolved in the present-day  
119 mantle as slabs below the southeastern Mediterranean Sea, central Arabia and the west Indian  
120 Ocean<sup>26</sup>.

121 East of Arabia, we trace the intra-oceanic plate boundary to a NE-SW striking, NW-  
122 dipping subduction zone between the Kabul Block and the west Indian passive margin. The 96  
123 Ma Waziristan ophiolites of Pakistan formed above this subduction zone and were thrust  
124 eastward onto the Indian continental margin<sup>13,16</sup> (Fig. 1B, C). This part of the plate boundary  
125 may have inverted a spreading ridge that formed between the Kabul Block and India in the Early  
126 Cretaceous<sup>13</sup>. The Cretaceous intra-Neotethyan plate boundary may have been convergent to as  
127 far south as the Amirante Ridge in the west Indian Ocean<sup>13</sup>, but there is no record of  
128 contemporaneous subduction beyond there. Instead, the plate boundary became extensional and  
129 developed a rift, and later a mid-oceanic ridge in the Mascarene Basin that accommodated  
130 separation of India from Madagascar<sup>13,27,28</sup> (Fig. 1B). The plate boundary ended in a ridge-ridge-  
131 ridge triple junction with ridges bordering the Antarctic plate in the south Indian Ocean<sup>13,28</sup> (Fig.  
132 1B).

133 The newly formed Cretaceous plate boundary essentially temporarily merged a large part  
134 of Neotethyan oceanic lithosphere between Arabia and Eurasia to the Indian plate. This plate was  
135 >12,000 km long from triple junction to triple junction, and reached from 45°S to 45°N, with  
136 4500 km of rift/ridge in the southeast and 7500 km of subduction zone in the northwest and with  
137 a transition between the convergent and divergent segments, representing the India-Africa Euler  
138 pole<sup>13</sup>, in the west Indian Ocean (Fig. 1B). Marine geophysical constraints show a ~4°  
139 counterclockwise rotation of India relative to Africa about the west Indian Ocean Euler pole  
140 during rifting preceding the ~83 Ma onset of oceanic spreading in the Mascarene Basin<sup>27-29</sup>,  
141 associated with up to hundreds of km of ~E-W convergence across the Neotethys (Fig. 1D).

142 The neighboring plates of the intra-Neotethyan subduction zone at 105 Ma were thus  
143 Africa and India. The African plate was mostly surrounded by ridges and had a complex  
144 subduction plate boundary in the Mediterranean region<sup>30</sup>. The Indian plate was surrounded by  
145 ridge-transform systems in the south and east and by subduction in the north, and may have  
146 contained rifts and ridges between the Indian continent and Eurasia<sup>13,28</sup>. The Neotethys  
147 lithosphere between Arabia-Greater Adria and Eurasia continued unbroken to the north-dipping

148 subduction zone that had already existed along the southern Eurasian margin since the  
149 Jurassic<sup>31,32</sup>; the spreading ridges that existed during Neotethys Ocean opening in the Permian-  
150 Triassic (north of Arabia)<sup>33</sup>, and Triassic-Jurassic (eastern Mediterranean region)<sup>23</sup> had already  
151 subducted below Eurasia by 105 Ma<sup>19,33</sup> (Fig. 1B, C).

152

### 153 **Identifying potential drivers of plate boundary formation**

154 Collisions, subduction relocations, or mantle plume arrivals around or within the Indian  
155 or African plates are all candidate processes to explain plate boundary formation at 105 Ma. At  
156 the northern boundary of between these plates and southern Eurasia, many collisions of  
157 microcontinents and arcs occurred since the Paleozoic, but none started or ended around 105  
158 Ma<sup>13,21-23,33-35</sup>. Continental subduction and collision was ongoing in the central Mediterranean  
159 region<sup>23</sup>, but it is not evident how this or any other changes in subduction dynamics along the E-  
160 W trending southern Eurasian margin would lead to E-W convergence in the Neotethys Ocean.  
161 In the eastern Neotethys, a mid-Cretaceous collision of the intra-oceanic Woyla Arc with the  
162 Sundaland continental margin led to a subduction polarity reversal initiating eastward subduction  
163 below Sundaland<sup>36</sup>, which is recorded in ophiolites on the Andaman Islands. There, metamorphic  
164 sole rocks with <sup>40</sup>Ar/<sup>39</sup>Ar hornblende cooling ages of 105-106 Ma, and likely coeval SSZ  
165 ophiolite spreading ages<sup>37</sup> reveal that this subduction zone may have developed slab pull around  
166 the same time as the Indian Ocean-western Neotethys plate boundary formed (Fig 1C). However,  
167 eastward slab pull below Sundaland cannot drive E-W convergence in the Neotethys to the west,  
168 and Andaman SSZ extension may well be an expression rather than the trigger of Indian plate  
169 rotation. Hence, we find no viable plate tectonics-related driver of the ~105 Ma plate boundary  
170 formation that we reconstructed here.

171 A key role, however, is possible for the only remaining geodynamic, non-plate-tectonic,  
172 plate-motion driver in the region: a mantle plume. India-Madagascar continental breakup is  
173 widely viewed<sup>13,27,37</sup> as related to the ~94 Ma and younger formation of the Morondava Large  
174 Igneous Province (LIP) on Madagascar<sup>38</sup> and southwest India<sup>39</sup>. This LIP, however, started  
175 forming ~10 Ma after initial plate boundary formation. To understand whether the plume may be  
176 responsible for both LIP emplacement and plate boundary formation, we conduct explorative  
177 torque-balance simulations of plume-lithosphere interaction.

178

## 179 **Mantle plumes driving plate boundary formation and subduction initiation**

180 Numerical simulations of plume-lithosphere interaction have already identified that  
181 plume head spreading below the lithosphere leads to horizontal asthenospheric flow that exerts a  
182 ‘plume push’ force on the base of the lithosphere, particularly in the presence of a cratonic  
183 keel<sup>5,40,41</sup>. Plume push may accelerate plates by several cm/yr<sup>41</sup> and has been proposed as a  
184 potential driver of subduction initiation<sup>5</sup>.

185 In many cases, including in the case of the Morondava LIP, LIP eruption and  
186 emplacement shortly preceded continental breakup, but pre-break up rifting preceded LIP  
187 emplacement by 10-15 Myr<sup>27</sup>. This early rifting typically is interpreted to indicate that the plume  
188 migrated along the base of the lithosphere into a pre-existing rift that formed independently of  
189 plume rise<sup>27</sup>. However, in numerical simulations dynamic uplift<sup>42</sup> and plume push<sup>41</sup> already start  
190 to accelerate plates 10-15 Myr before the plume head reaches the base of the lithosphere and  
191 emplaces the LIP. Numerical simulations thus predict the observed delay between plume push,  
192 as a driver for early rifting and subduction initiation, and LIP eruption and emplacement.

193 Here, we add to these plume-lithosphere coupling experiments by conducting proof-of-  
194 concept torque-balance simulations particularly exploring why the observed India-Africa Euler  
195 pole is so close to the plume head such that the associated plate rotation between Africa and  
196 India caused E-W convergence in the Neotethys. We performed semi-analytical computations,  
197 including both the Indian and African plates at ~105 Ma, and assess the influence of cratonic  
198 keels on the position of the India-Africa Euler pole (Fig. 2, see Methods).

199 In our computations without cratonic keels, plume push under Madagascar/India caused  
200 counterclockwise rotation of India versus Africa, but about an Euler pole situated far north of  
201 Arabia, (Fig. 2A) without inducing significant E-W convergence within the Neotethys. However,  
202 in experiments that include keels of the Indian and African cratonic lithosphere, which are  
203 strongly coupled to the sub-asthenospheric mantle, the computed Euler pole location is shifted  
204 southward towards the Indian continent, inducing E-W convergence along a larger part of the  
205 plate boundary within the Neotethys Ocean (Fig. 2B).

206 Convergence of up to several hundreds of km, sufficient to induce self-sustaining  
207 subduction<sup>27</sup>, is obtained if plume material is fed into – and induced flow is confined to – a 200  
208 km thick weak asthenospheric layer. The thinner this layer is, the further the plume head spreads,  
209 and pushes the plate. The modern Indian cratonic root used in our computations has likely eroded  
210 considerably during interaction with the ~70-65 Ma Deccan plume<sup>43</sup>. India may have had a  
211 thicker and/or laterally more extensive cratonic root at ~105 Ma than modeled here which would  
212 further enhance coupling of the lithosphere and the sub-asthenospheric mantle. Furthermore, an  
213 Euler pole close to India and a long convergent boundary to the north requires much weaker  
214 coupling in the northern (oceanic) part of the India plate (Fig. 2). In this case, results remain  
215 similar as long as the plume impinges near the southern part of the western boundary of  
216 continental India.

217 An order of magnitude estimate of the maximum plume-induced stresses, assuming no  
218 frictional resistance at other plate boundaries, is obtained from the rising force of  $\sim 1.5 \cdot 10^{20}$  N of  
219 a plume head with 1000 km diameter and density contrast  $30 \text{ kg/m}^3$ . If half of this force acts on  
220 the India plate and with a lever arm of 4000 km, this corresponds to a torque of  $3 \cdot 10^{26}$  Nm. Once,  
221 at the onset of rifting, ridge push is established as an additional force in the vicinity of the plume,  
222 we estimate that this number may increase by up to a few tens of per cent. This torque can be  
223 balanced at the convergent boundary (length  $\sim 5000$  km, plate thickness  $\sim 100$  km) involving  
224 stresses of  $\sim 240$  MPa, much larger than estimates of frictional resistance between subducting and  
225 overriding plates that are only of the order of tens of MPa<sup>44</sup>. For this estimate, we neglect any  
226 frictional resistance at the base of the plate and at any other plate boundary – essentially  
227 considering the plate as freely rotating above a pinning point. This is another endmember  
228 scenario, as opposed to our above convergence estimate, where we had considered friction at the  
229 plate base but neglected it at all plate boundaries. Therefore, the estimate of 240 MPa may be  
230 considered as an upper bound but being compressive and oriented in the right direction it shows  
231 the possibility of subduction initiation as has occurred in reality along the likely weakened  
232 passive margin region of Arabia and Greater Adria. Moreover, the plume-induced compressive  
233 stresses may have added to pre-existing compressive stresses, in particular due to ridge-push  
234 around the African and Indian plates. Such additional compressive stresses may contribute to  
235 shifting the Euler pole further south, closer to the position reconstructed in Fig. 1.



236 Subduction became self-sustained ~8-12 Ma after its initiation, as marked by the 96-92  
237 Ma age of SSZ spreading<sup>15,17</sup>: inception of this spreading shows that subduction rates exceeded  
238 convergence rates, and reconstructed SSZ spreading rates were an order of magnitude higher<sup>15</sup>  
239 than Africa-Arabia or Indian absolute plate motions<sup>41,45</sup> signaling slab roll-back, i.e. self-  
240 sustained subduction<sup>20,46</sup>. Numerical models suggest that self-sustained subduction may start  
241 after ~50-100 km of induced convergence<sup>7</sup>, corresponding to ~1° of India-Africa rotation  
242 between ~105 and ~96-92 Ma. Subsequent east and west-dipping subduction segments (Fig. 1)  
243 may have contributed to and accelerated the India-Africa/Arabia rotation, driving the  
244 propagation of the Euler pole farther to the south (compare Fig. 2A, C).

245

### 246 **Mantle plumes as an initiator of plate tectonics?**

247 Previously, numerical modeling has shown that mantle plumes may trigger circular  
248 subduction initiation around a plume head<sup>4</sup>, where local plume-related convection may drive  
249 subduction of thermally weakened lithosphere. This subduction would propagate through slab  
250 roll-back and may have started the first subduction features on Earth<sup>4</sup>. 3D convective models do  
251 produce a global network of plate boundaries<sup>47,48</sup> but the role of plumes in initiating new  
252 subduction zones within this network is unclear. Here, we have provided the first evidence that  
253 plume rise formed a >12,000 km long plate boundary composed of both convergent and  
254 divergent segments. Our documented example is Cretaceous in age but geological observations  
255 showing a general temporal overlap between LIP emplacement and formation of SSZ ophiolite  
256 belts over more than a billion years<sup>49</sup> suggest that plume rise is a key driving factor in the  
257 formation of subduction plate boundaries. Because mantle plumes are thought to be also  
258 common features on planets without plate tectonics, such as Mars and Venus<sup>50</sup>, they may have  
259 played a vital role in the emergence of modern style plate tectonics on Earth. That plumes may  
260 have been key for the evolution of plate tectonics on Earth, as we suggest, but apparently  
261 insufficient on Mars and Venus, provides a new outlook on understanding the different planetary  
262 evolutions.

263

264 **Acknowledgments:** DJJvH, MM, DG, AP, and ELA were funded through European Research  
265 Council Starting Grant 306810 (SINK) to DJJvH. DJJvH, KP and PJMcP were funded

266 through Netherlands Organization for Scientific Research (NWO) Vidi grant 864.11.004  
267 to DJJvH. DJJvH acknowledges Netherlands Organization for Scientific Research  
268 (NWO) Vici grant 865.17.001. BS and CGa received funding from the Research Council  
269 of Norway through its Centres of Excellence funding scheme, project number 223272.  
270 BS received additional funding from the innovation pool of the Helmholtz Association  
271 through the “Advanced Earth System Modelling Capacity (ESM)” activity. CG was  
272 funded through Discovery Grant (RGPIN-2014-05681) from the National Science and  
273 Engineering Research Council of Canada. We thank Inge Loes ten Kate and Debaditya  
274 Bandyopadhyay for discussion, and Fabio Capitanio, Dietmar Müller, and an anonymous  
275 reviewer for their constructive comments.

276

277 **Author contributions:** DJJvH, BS, WS designed research. DJJvH, CGu, MM, DG, KP, AP,  
278 PJmcP, CGa, ELA and RLMV developed the kinematic reconstruction; BS performed  
279 modelling; DJJvH, BS, CGu, WS wrote the paper, all authors made corrections and edits.

280

281 **Competing interests:** All authors declare no competing interests.

282

283

284 **Fig. 1.** Plate kinematic reconstructions of the Neotethys Ocean and surrounding continents at A)  
285 the present-day; B) 70 Ma, corresponding to the time that most of the Neotethyan intra-oceanic  
286 subduction zone had terminated due to arrival of the India, Africa-Arabia, and the Greater Adria  
287 margin in the trench; C) 105 Ma, corresponding to the timing of intra-Neotethyan subduction  
288 initiation and D) 110 Ma, just before intra-Neotethyan subduction initiation. An Euler pole  
289 situated in the Indian Ocean north of Madagascar (yellow star) indicates the division between the  
290 compressional plate boundary segment (the intra-Neotethys trench) and the extensional segment  
291 (the incipient Mascarene rift connected to the mid-ocean ridge between Africa and Antarctica).  
292 Rotation around this pole, and the related intra-Neotethyan subduction initiation, are interpreted  
293 here to result from the rise and push of the Morondava mantle plume. See text for further  
294 explanation, and Methods for the plate reconstruction approach and sources of detailed  
295 restorations. Dark grey areas outline modern continents; light-grey areas indicate thinned  
296 continental margins and microcontinents. Grey arrows indicate approximate rotational motion in  
297 a mantle reference frame<sup>45</sup> around the Amirante Euler pole. AR = Amirante Ridge; Emed =  
298 Eastern Mediterranean Region; Ir = Iran; LIP = Large Igneous Province; Mad = Madagascar;  
299 Mas = Mascarene Basin; Pak = Pakistan, Tur = Turkey; Waz = Waziristan Ophiolite.

300

301 **Fig. 2.** The computed total displacement, induced by the Morondava plume (pink circle) for the  
302 restored ~105 Ma plate configuration (Fig. 1C) for plates without (A, B) and with (C, D) African  
303 and Indian cratonic keels, in an Africa-fixed (A, C), or mantle reference frame<sup>45</sup> (B, D) (see  
304 Methods). It is assumed that, compared to a case with no lateral variations, the drag force due to  
305 the plate moving over the mantle is increased by a factor of ten wherever reconstructed  
306 lithosphere thickness exceeds 100 km (brown areas) and reduced to one tenth of the drag force  
307 wherever it is less than 100 km thick. The India craton hence nearly “pins” the India plate, such  
308 that its northern part moves in the opposite direction to the plume-induced push. Computation  
309 assumes torque balance between plume push and shearing over asthenosphere; frictional  
310 resistance at plate boundaries is neglected and computed convergence of several hundred km at  
311 the northern end of the plate boundary is a maximum estimate. Ten degree grid spacing;

312 locations of plates, lithosphere thickness and the plume are reconstructed in a slab-fitted mantle  
313 reference frame<sup>45</sup>.

314

315         **Methods: Kinematic reconstruction** – The kinematic restoration of Neotethyan intra-  
316 oceanic subduction was made in GPlates plate reconstruction software ([www.gplates.org](http://www.gplates.org))<sup>51</sup>.  
317 First, we systematically restored stable plates using marine geophysical data from the Atlantic  
318 and Indian Ocean, and then restored continental margin deformation that occurred following the  
319 arrival of continental lithosphere below the oceanic lithosphere preserved as ophiolites. These  
320 restorations are based on a systematic reconstruction protocol, based on magnetic anomalies and  
321 fracture zones of present-day sea floor and geophysical constraints on pre-drift extension in  
322 adjacent passive continental margins<sup>23</sup>, followed by kinematic restoration of post-obduction  
323 orogenic deformation using structural geological constraints on continental extension, strike-slip  
324 deformation, and shortening, and paleomagnetic constraints on vertical axis rotations. We then  
325 restored pre-emplacement vertical axis microplate rotations<sup>52,53</sup>, as well as paleo-orientations of  
326 the SSZ spreading ridges at which the ophiolitic crust formed<sup>18-20</sup>. The reconstruction shown in  
327 Fig. 1B compiles kinematic restorations for the eastern Mediterranean region<sup>23</sup>, Iran<sup>54</sup>, Oman<sup>20</sup>,  
328 Pakistan<sup>13</sup>, and the Himalaya<sup>34</sup>. Ophiolites interpreted to be part of the Cretaceous subduction  
329 system include the 96-90 Ma, Cretaceous ophiolites exposed in SE Greece, Anatolia, Cyprus,  
330 Syria, and Iraq, the Neyriz ophiolite of Iran, the Semail ophiolite in Oman, and the Waziristan-  
331 Khost ophiolite in Pakistan and Afghanistan<sup>15-17,55</sup>. The Jurassic ophiolite belts of northern  
332 Turkey and Armenia<sup>56-58</sup> and the late Cretaceous (<80 Ma) Kermanshah ophiolite of Iran<sup>59</sup> are  
333 not included and are instead interpreted to have formed along the southern Eurasian margin<sup>23</sup>.  
334 The Masirah Ophiolite of East Oman<sup>60</sup> and the uppermost Cretaceous Bela, Muslim Bagh, and  
335 Kabul-Altumur ophiolites of Pakistan and Afghanistan<sup>61,62</sup> are interpreted to reflect oblique latest  
336 Cretaceous to Paleogene India-Arabia convergence<sup>13</sup> and are also unrelated to the event studied  
337 here. Restoration of intra-oceanic subduction prior to the arrival of the continental margins used  
338 paleomagnetic data from the ophiolites of Oman, Syria, Cyprus, and Turkey that constrain  
339 vertical axis rotations, as well as the orientation of sheeted dyke following cooling after  
340 intrusion<sup>18-20,52,53</sup> as proxy for original ridge and intra-oceanic trench orientations. These  
341 paleomagnetic data systematically revealed N-S to NW-SE primary sheeted dyke orientations<sup>18-</sup>

342 20,52,53. Because the ages of the SSZ ophiolites in the Neotethyan belt do not laterally progress,  
343 spreading must have occurred near-orthogonal to the associated trench, which must thus also  
344 have been striking N-S to NE-SW, as shown in the reconstruction of Fig. 1.

345 How far the Indian plate continued northwards around 105 Ma is subject to ongoing  
346 debate. On the one hand, the northern Indian continental margin has been proposed to have rifted  
347 off India sometime in the Cretaceous<sup>34,63</sup>, but recent paleomagnetic data suggest that this process  
348 occurred in the late Cretaceous, well after 100 Ma<sup>64</sup>. Others inferred that the north Indian  
349 continent had a passive margin contiguous with oceanic Neotethyan lithosphere since the middle  
350 Jurassic or before and continued to a subduction zone below the SSZ ophiolites found in the  
351 Himalayan suture zone and the Kohistan arc<sup>35,65,66</sup>. Sedimentary and paleomagnetic data  
352 demonstrate that these ophiolites formed adjacent to the Eurasian margin in the Early  
353 Cretaceous<sup>67</sup>, although they may have migrated southward during slab roll-back in the Late  
354 Cretaceous<sup>35</sup>. Recent paleomagnetic data have shown that a subduction zone may have existed  
355 within the Neotethys to the west of the Andaman Islands, above which the West Burma Block  
356 would have been located (Figure 1)<sup>68</sup>. Our reconstruction of the eastern Neotethys may thus be  
357 oversimplified. However, the geological record of the West Burma Block shows that this  
358 subduction zone already existed as early as 130 Ma, and E-W trending until well into the  
359 Cenozoic<sup>68</sup>, and we see no reason to infer that changes in the eastern Neotethys contributed to  
360 the plate boundary formation discussed here. Some have speculated that the West Burma  
361 subduction zone would have been connected to a long-lived, equatorial subduction zone within  
362 the Neotethys all along the Indian segment that would already have existed in the Early  
363 Cretaceous<sup>69</sup>: this scenario remains unconstrained by paleomagnetic data, and is inconsistent  
364 with sediment provenance data from the Himalaya and overlying ophiolites<sup>35</sup>. In summary, the  
365 Indian plate around 105 Ma continued far into the Neotethyan realm, and the India-Africa  
366 rotation is a likely driver of E-W convergence sparking subduction initiation close to the  
367 northern Gondwana margin purported in Figure 1.

368 *Torque balance modeling* – Forces considered here include (i) the push due to plume-  
369 induced flow in the asthenosphere and (ii) the drag due to shear flow between the moving plate  
370 and a deeper mantle at rest (Fig. S1). In the first case, we disregard any lateral variations. Plume-  
371 induced flow is treated as Poiseuille flow, i.e. with parabolic flow profile, in an asthenospheric  
372 channel of thickness  $h_c$ , radially away from the plume stem. Since at greater distance plume-

373 induced flow will eventually not remain confined to the asthenosphere, we only consider it to a  
 374 distance 2400 km, in accord with numerical results<sup>41</sup>, and consistent with the finding that there is  
 375 a transition from dominantly pressure-driven Poiseuille flow at shorter wavelengths to  
 376 dominantly shear-driven Couette flow at length scales approximately exceeding mantle  
 377 depth<sup>70,71</sup>. With  $v_0$  the velocity in the center of the channel at a distance  $d$  from the plume stem  
 378 the total volume flux rate is  $2/3 \cdot v_0 \cdot 2\pi d \cdot h_c$  (here neglecting the curvature of the Earth surface  
 379 for simplicity). Its time integral is equal to the volume of the plume head with radius estimated<sup>72</sup>  
 380 to be about  $r_p=500$  km, with considerable uncertainty. That is, integration is done over a time  
 381 interval until the entire plume head volume has flown into the asthenospheric channel. Hence the  
 382 corresponding displacement vector in the center of the channel is

$$\mathbf{x}_{plu} = \int_{\Delta t} v_0 dt \cdot \mathbf{e}_r = \frac{r_p^3}{d \cdot h_c} \cdot \mathbf{e}_r$$

383  
 384 where  $\mathbf{e}_r$  is the unit vector radially away from the plume (red arrows in Extended Data Fig. 1).  
 385 Because of the parabolic flow profile, the vertical displacement gradient at the top of the channel  
 386 is

$$2 \cdot \frac{\mathbf{x}_{plu}}{0.5 \cdot h_c} = 2 \cdot \int_{\Delta t} v_0 dt \cdot \frac{1}{0.5 \cdot h_c} \cdot \mathbf{e}_r = \frac{4r_p^3}{d \cdot h_c^2} \cdot \mathbf{e}_r.$$

387  
 388 Viscosity is defined such that the force per area is equal to viscosity times the radial gradient of  
 389 horizontal velocity. Hence the time integral of torque on the plate is

$$\mathbf{T}_{plu} = \frac{4\eta_0}{h_c} \int_A \mathbf{r} \times \mathbf{x}_{plu} dA = \frac{4\eta_0 r_p^3}{d \cdot h_c^2} \int_A \mathbf{r} \times \mathbf{e}_r dA$$

390  
 391 where  $\eta_0$  is viscosity in the channel and  $\mathbf{r}$  is the position vector.  $\mathbf{T}_{plu}$  is balanced by the time-  
 392 integrated torque  $\mathbf{T}_{pla}$  of the plate rotating an angle  $\omega$  over the underlying mantle. With plate  
 393 displacement vectors  $\mathbf{x}_{pla} = \omega \times \mathbf{r}$  (black arrows in Fig. S1) we obtain

$$\mathbf{T}_{pla} = -\frac{\eta_0}{h_s} \int_A \mathbf{r} \times \mathbf{x}_{pla} dA = -\frac{\eta_0}{h_s} \int_A \mathbf{r} \times (\omega \times \mathbf{r}) dA$$

394

395 Here  $h_s$  is an effective thickness of the layer over which shearing occurs, which is calculated  
 396 below for a stratified viscosity structure, i.e. laterally homogeneous coupling of plate and mantle  
 397 and which we will set equal to  $h_c$  for simplicity. Specifically, with  $\mathbf{T}_x$  being the time-integrated  
 398 torque acting on a plate rotating an angle  $\omega_0$  around the x-axis

$$\mathbf{T}_x = -\frac{\omega_0 \eta_0}{h_s} \int_A \mathbf{r} \times (\mathbf{e}_x \times \mathbf{r}) dA,$$

399

400 and  $\mathbf{T}_y$  and  $\mathbf{T}_z$  defined in analogy, the torque balance equation can be written

$$\mathbf{T}_{plu} = \frac{\omega_x}{\omega_0} \cdot \mathbf{T}_x + \frac{\omega_y}{\omega_0} \cdot \mathbf{T}_y + \frac{\omega_z}{\omega_0} \cdot \mathbf{T}_z$$

401

402  $\omega_0$  cancels out when  $\mathbf{T}_x$ ,  $\mathbf{T}_y$  and  $\mathbf{T}_z$  are inserted. Integrals used to compute these torques only  
 403 depend on plate geometry,  $\eta_0$  cancels out in the torque balance, and we can solve for the rotation  
 404 angle vector  $\boldsymbol{\omega}$  simply by a 3 x 3 matrix inversion. In the more general case, where we do not set  
 405  $h_s$  and  $h_c$  equal,  $\boldsymbol{\omega}$  is scaled by a factor  $h_s/h_c$ .

406 If a plate moves over a mantle where viscosity varies with depth, then the force per area  
 407  $F/A$  should be the same at all depths, and the radial gradient of horizontal velocity  $dv/dz = F/A \cdot$   
 408  $1/\eta(z)$ . If we assume that the deep mantle is at rest (i.e. it moves slowly compared to plate  
 409 motions), we further find that plate motion is

$$v_0 = \int_{z_0}^{z(\eta_{\max})} \frac{dv}{dz} dz = \frac{F}{A} \int_{z_0}^{z(\eta_{\max})} \frac{1}{\eta(z)} dz =: \frac{F h_s}{A \eta_0} \quad (1)$$

410

411 The integration is done from the base of the lithosphere  $z_0$  to the depth where the approximation  
 412 of the “mantle at rest” is probably the most closely matched, i.e. we choose the viscosity  
 413 maximum. The last equality is according to the definition of the effective layer thickness,  
 414 whereby  $\eta_0$  is the viscosity just below the lithosphere. Solving this equation for  $h_s$  for the  
 415 viscosity structure in Extended Data Fig. 2 and a 100 km thick lithosphere gives  $h_s=203.37$  km.

416 The plume location at 27.1°E, 40.4° S, is obtained by rotating the center of the  
 417 corresponding LIP at 46° E, 26° S and an age 87 Ma (adopted from Doubrovine et al.<sup>73</sup>) in the

418 slab-fitted mantle reference frame<sup>45</sup>, in which also the plate geometries at 105 Ma are  
419 reconstructed.

420 Results for this case (Fig. 2A) show that a plume pushing one part of a plate may induce  
421 a rotation of that plate, such that other parts of that plate may move in the opposite direction. A  
422 simple analog is a sheet of paper pushed, near its bottom left corner, to the right: Then, near the  
423 top left corner, the sheet will move to the left. With two sheets (plates) on either side, local  
424 divergence near the bottom (near the plume) may turn into convergence near the top (at the part  
425 of the plate boundary furthest away from the plume). The length of that part of the plate  
426 boundary, where convergence is induced may increase, if one plate is nearly “pinned” at a hinge  
427 point slightly NE of the plume, perhaps due to much stronger coupling between plate and mantle.  
428 At the times considered here ~105 My ago, the Indian continent, where coupling was presumably  
429 stronger, was in the southern part of the Indian plate, whereas in its north, there was a large  
430 oceanic part, with presumably weaker coupling. Hence the geometry was indeed such that  
431 convergence could be induced along a longer part of the plate boundary.

432 In the second case, we therefore consider lateral variations in the coupling between plate  
433 and mantle, corresponding to variations in lithosphere thickness and/or asthenosphere viscosity,  
434 by multiplying the drag force (from the first case) at each location with a resistance factor. This  
435 factor is a function of lithosphere thickness reconstructed at 105 Ma. On continents, thickness  
436 derived from tomography<sup>74</sup> with slabs removed<sup>75</sup> is simply backward-rotated. In the oceans, we  
437 use thickness [km] =  $10 \cdot (\text{age [Ma]} - 105)^{0.5}$  with ages from present-day Earthbyte age grid  
438 version 3.6, i.e. accounting for the younger age and reduced thickness at 105 Ma, besides  
439 backward-rotating. To determine the appropriate rotation, the lithosphere (in present-day  
440 location) is divided up into India, Africa, Arabia, Somalia and Madagascar (paleo-)plates and  
441 respective 105 Ma finite rotations from van der Meer et al.<sup>45</sup> are applied. For the parts of the  
442 reconstructed plates where thickness could not be reconstructed in this way – often, because this  
443 part of the plate has been subducted – we first extrapolate thickness up to a distance ~2.3°, and  
444 set the thickness to a default value of 80 km for the remaining part. Reconstructed thickness is  
445 shown in Extended Data Fig. 4. For the resistance factor as a function of lithosphere thickness  
446 we use two models: Firstly, we use a continuous curve (Extended Data Fig. 3) according to eq.  
447 (1)



$$\frac{F}{A} = \frac{v_0}{\int_{z_0}^{z(\eta_{\max})} \frac{1}{\eta(z)} dz}. \quad (2)$$

448

449 with the mantle viscosity model in Extended Data Fig. 2 combined with variable lithosphere  
450 thickness  $z_0$ . However, this causes only a minor change in the plate rotations (Extended Data Fig.  
451 4 compared to Fig. 2B). Hence, we also use a stronger variation, further explained in the caption  
452 of Fig 2 and with results shown in Fig. 2C and D.

453

#### 454 **Data availability**

455 GPlates files with reconstructions used to draft Figure 1 are provided at  
456 [https://figshare.com/articles/dataset/van\\_Hinsbergen\\_NatureGeo\\_2021\\_GPlates\\_zip/13516727](https://figshare.com/articles/dataset/van_Hinsbergen_NatureGeo_2021_GPlates_zip/13516727).

457

#### 458 **Code availability**

459 All codes used in the geodynamic modeling in this study are available at  
460 [https://figshare.com/articles/software/van\\_Hinsbergen\\_etal\\_NatureGeo\\_2021\\_geodynamics\\_package/13635089](https://figshare.com/articles/software/van_Hinsbergen_etal_NatureGeo_2021_geodynamics_package/13635089).

462

463

464 **References:**

- 465 1 Lenardic, A. The diversity of tectonic modes and thoughts about transitions between them. *Philosophical*  
 466 *Transactions of the Royal Society A: Mathematical, Physical and Engineering Sciences* **376**, 20170416  
 467 (2018).
- 468 2 Stern, R. J. Subduction initiation: spontaneous and induced. *Earth and Planetary Science Letters* **226**, 275-  
 469 292, doi:10.1016/s0012-821x(04)00498-4 (2004).
- 470 3 Hall, C. E., Gurnis, M., Sdrolias, M., Lavier, L. L. & Müller, R. D. Catastrophic initiation of subduction  
 471 following forced convergence across fracture zones. *Earth and Planetary Science Letters* **212**, 15-30,  
 472 doi:10.1016/s0012-821x(03)00242-5 (2003).
- 473 4 Gerya, T. V., Stern, R. J., Baes, M., Sobolev, S. V. & Whattam, S. A. Plate tectonics on the Earth triggered  
 474 by plume-induced subduction initiation. *Nature* **527**, 221-225, doi:10.1038/nature15752 (2015).
- 475 5 Pusok, A. E. & Stegman, D. R. The convergence history of India-Eurasia records multiple subduction  
 476 dynamics processes. *Science Advances* **6**, eaaz8681 (2020).
- 477 6 Baes, M., Sobolev, S., Gerya, T. & Brune, S. Plume-Induced Subduction Initiation: Single-Slab or Multi-  
 478 Slab Subduction? *Geochemistry, Geophysics, Geosystems* **21**, e2019GC008663 (2020).
- 479 7 Gurnis, M., Hall, C. & Lavier, L. Evolving force balance during incipient subduction. *Geochemistry,*  
 480 *Geophysics, Geosystems* **5**, doi:10.1029/2003gc000681 (2004).
- 481 8 Guilmette, C. *et al.* Forced subduction initiation recorded in the sole and crust of the Semail Ophiolite of  
 482 Oman. *Nature Geoscience* **11**, 688-695 (2018).
- 483 9 Stern, R. J. & Gerya, T. Subduction initiation in nature and models: A review. *Tectonophysics*,  
 484 doi:10.1016/j.tecto.2017.10.014 (2017).
- 485 10 Agard, P. *et al.* Plate interface rheological switches during subduction infancy: Control on slab penetration  
 486 and metamorphic sole formation. *Earth and Planetary Science Letters* **451**, 208-220 (2016).
- 487 11 van Hinsbergen, D. J. J. *et al.* Dynamics of intraoceanic subduction initiation: 2. Suprasubduction zone  
 488 ophiolite formation and metamorphic sole exhumation in context of absolute plate motions. *Geochemistry,*  
 489 *Geophysics, Geosystems* **16**, 1771-1785, doi:10.1002/2015gc005745 (2015).
- 490 12 Dilek, Y. & Furnes, H. Ophiolite genesis and global tectonics: Geochemical and tectonic fingerprinting of  
 491 ancient oceanic lithosphere. *Geological Society of America Bulletin* **123**, 387-411, doi:10.1130/b30446.1  
 492 (2011).
- 493 13 Gaina, C., van Hinsbergen, D. J. J. & Spakman, W. Tectonic interactions between India and Arabia since  
 494 the Jurassic reconstructed from marine geophysics, ophiolite geology, and seismic tomography. *Tectonics*  
 495 **34**, 875-906, doi:10.1002/2014tc003780 (2015).
- 496 14 Pourteau, A. *et al.* Thermal evolution of an ancient subduction interface revealed by Lu–Hf garnet  
 497 geochronology, Halilbağ Complex (Anatolia). *Geoscience Frontiers* **10**, 127-148,  
 498 doi:10.1016/j.gsf.2018.03.004 (2019).
- 499 15 Rioux, M. *et al.* Synchronous formation of the metamorphic sole and igneous crust of the Semail ophiolite:  
 500 New constraints on the tectonic evolution during ophiolite formation from high-precision U–Pb zircon  
 501 geochronology. *Earth and Planetary Science Letters* **451**, 185-195 (2016).
- 502 16 Robinson, J., Beck, R., Gnos, E. & Vincent, R. K. New structural and stratigraphic insights for  
 503 northwestern Pakistan from field and Landsat Thematic Mapper data. *Geological Society of America*  
 504 *Bulletin* **112**, 364-374, doi:10.1130/0016-7606(2000)112<364:Nsasif>2.0.Co;2 (2000).
- 505 17 Parlak, O. The tauride ophiolites of Anatolia (Turkey): A review. *Journal of Earth Science* **27**, 901-934,  
 506 doi:10.1007/s12583-016-0679-3 (2016).
- 507 18 van Hinsbergen, D. J. J. *et al.* Tectonic evolution and paleogeography of the Kırşehir Block and the Central  
 508 Anatolian Ophiolites, Turkey. *Tectonics* **35**, 983-1014, doi:10.1002/ (2016).
- 509 19 Maffione, M., van Hinsbergen, D. J. J., de Gelder, G. I. N. O., van der Goes, F. C. & Morris, A. Kinematics  
 510 of Late Cretaceous subduction initiation in the Neo-Tethys Ocean reconstructed from ophiolites of Turkey,  
 511 Cyprus, and Syria. *Journal of Geophysical Research: Solid Earth* **122**, 3953-3976,  
 512 doi:10.1002/2016jb013821 (2017).
- 513 20 van Hinsbergen, D. J., Maffione, M., Koornneef, L. M. & Guilmette, C. Kinematic and paleomagnetic  
 514 restoration of the Semail ophiolite (Oman) reveals subduction initiation along an ancient Neotethyan  
 515 fracture zone. *Earth and Planetary Science Letters* **518**, 183-196 (2019).
- 516 21 Torsvik, T. H. & Cocks, L. R. M. *Earth history and palaeogeography*. 317 (Cambridge University Press,  
 517 2017).

518 22 Wan, B. *et al.* Cyclical one-way continental rupture-drift in the Tethyan evolution: Subduction-driven plate  
519 tectonics. *Science China Earth Sciences*, 1-12 (2019).

520 23 van Hinsbergen, D. J. J. *et al.* Orogenic architecture of the Mediterranean region and kinematic  
521 reconstruction of its tectonic evolution since the Triassic. *Gondwana Research* **81**, 79-229 (2020).

522 24 Warren, C. J., Parrish, R. R., Waters, D. J. & Searle, M. P. Dating the geologic history of Oman's Semail  
523 ophiolite: insights from U-Pb geochronology. *Contributions to Mineralogy and Petrology* **150**, 403-422,  
524 doi:10.1007/s00410-005-0028-5 (2005).

525 25 Güngör, T. *et al.* Kinematics and U-Pb zircon ages of the sole metamorphics of the Marmaris Ophiolite,  
526 Lycian Nappes, Southwest Turkey. *International Geology Review* **61**, 1124-1142 (2019).

527 26 van der Meer, D. G., van Hinsbergen, D. J. J. & Spakman, W. Atlas of the underworld: Slab remnants in  
528 the mantle, their sinking history, and a new outlook on lower mantle viscosity. *Tectonophysics* **723**, 309-  
529 448, doi:10.1016/j.tecto.2017.10.004 (2018).

530 27 Buitter, S. J. & Torsvik, T. H. A review of Wilson Cycle plate margins: A role for mantle plumes in  
531 continental break-up along sutures? *Gondwana Research* **26**, 627-653 (2014).

532 28 Gibbons, A. D., Whittaker, J. M. & Müller, R. D. The breakup of East Gondwana: Assimilating constraints  
533 from Cretaceous ocean basins around India into a best-fit tectonic model. *Journal of Geophysical*  
534 *Research: Solid Earth* **118**, 808-822, doi:10.1002/jgrb.50079 (2013).

535 29 Gaina, C., Müller, R. D., Brown, B., Ishihara, T. & Ivanov, S. Breakup and early seafloor spreading  
536 between India and Antarctica. *Geophysical Journal International* **170**, 151-169, doi:10.1111/j.1365-  
537 246X.2007.03450.x (2007).

538 30 Gaina, C. *et al.* The African Plate: A history of oceanic crust accretion and subduction since the Jurassic.  
539 *Tectonophysics* **604**, 4-25, doi:10.1016/j.tecto.2013.05.037 (2013).

540 31 Agard, P., Jolivet, L., Vrielynck, B., Burov, E. & Monié, P. Plate acceleration: The obduction trigger?  
541 *Earth and Planetary Science Letters* **258**, 428-441, doi:10.1016/j.epsl.2007.04.002 (2007).

542 32 Jolivet, L. *et al.* Neo-Tethys geodynamics and mantle convection: from extension to compression in Africa  
543 and a conceptual model for obduction. *Canadian journal of earth sciences* **53**, 1190-1204 (2015).

544 33 Stampfli, G. M. & Borel, G. A plate tectonic model for the Paleozoic and Mesozoic constrained by  
545 dynamic plate boundaries and restored synthetic oceanic isochrons. *Earth and Planetary Science Letters*  
546 **196**, 17-33 (2002).

547 34 van Hinsbergen, D. J. J. *et al.* Reconstructing Greater India: Paleogeographic, kinematic, and geodynamic  
548 perspectives. *Tectonophysics* **760**, 69-94, doi:10.1016/j.tecto.2018.04.006 (2019).

549 35 Kapp, P. & DeCelles, P. G. Mesozoic–Cenozoic geological evolution of the Himalayan-Tibetan orogen and  
550 working tectonic hypotheses. *American Journal of Science* **319**, 159-254 (2019).

551 36 Advokaat, E. L. *et al.* Early Cretaceous origin of the Woyla Arc (Sumatra, Indonesia) on the Australian  
552 plate. *Earth and Planetary Science Letters* **498**, 348-361 (2018).

553 37 Plunder, A. *et al.* History of subduction polarity reversal during arc-continent collision: constraints from the  
554 Andaman Ophiolite and its metamorphic sole. *Tectonics*, e2019TC005762 (2020).

555 38 Torsvik, T. *et al.* Late Cretaceous magmatism in Madagascar: palaeomagnetic evidence for a stationary  
556 Marion hotspot. *Earth and Planetary Science Letters* **164**, 221-232 (1998).

557 39 Mohan, M. R. *et al.* The Ezhimala igneous complex, southern India: Possible imprint of late Cretaceous  
558 magmatism within rift setting associated with India–Madagascar separation. *Journal of Asian Earth*  
559 *Sciences* **121**, 56-71 (2016).

560 40 Cande, S. C. & Stegman, D. R. Indian and African plate motions driven by the push force of the Reunion  
561 plume head. *Nature* **475**, 47-52, doi:10.1038/nature10174 (2011).

562 41 van Hinsbergen, D. J. J., Steinberger, B., Doubrovine, P. V. & Gassmöller, R. Acceleration and  
563 deceleration of India-Asia convergence since the Cretaceous: Roles of mantle plumes and continental  
564 collision. *Journal of Geophysical Research* **116**, doi:10.1029/2010jb008051 (2011).

565 42 Wang, Y. & Li, M. The interaction between mantle plumes and lithosphere and its surface expressions: 3-D  
566 numerical modelling. *Geophysical Journal International*, doi:10.1093/gji/ggab014 (2021).

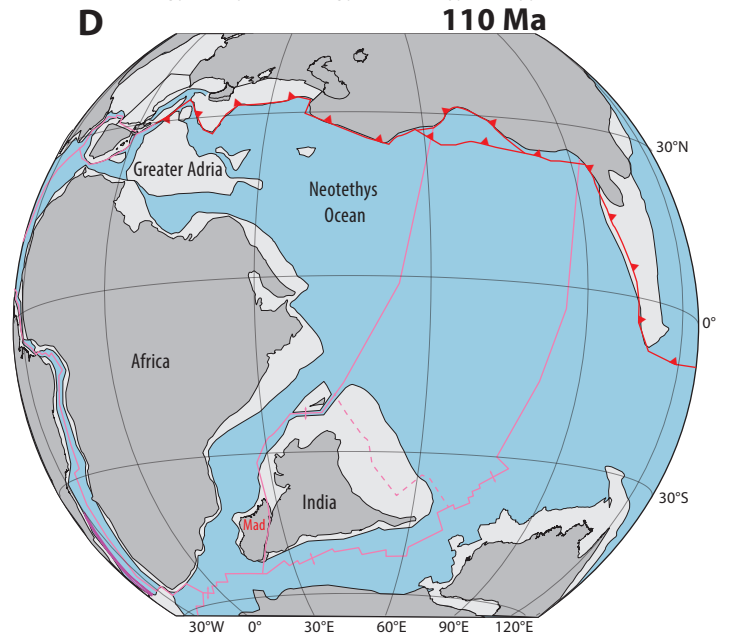
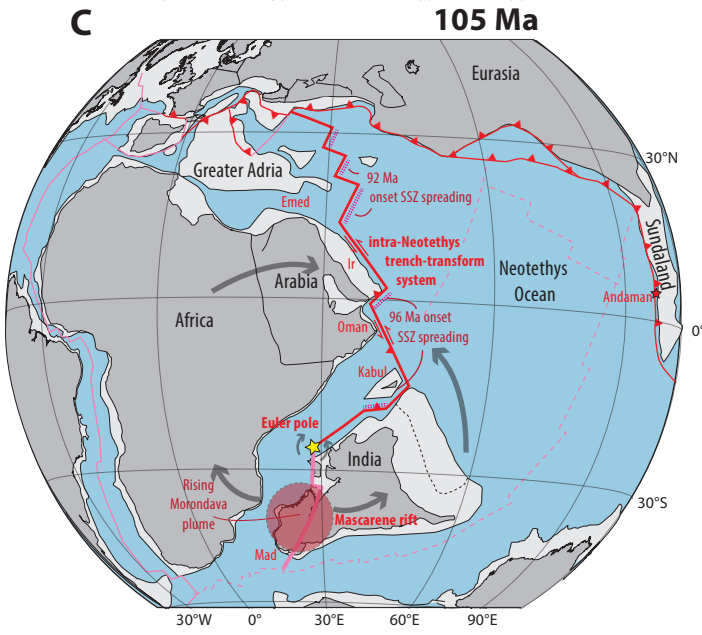
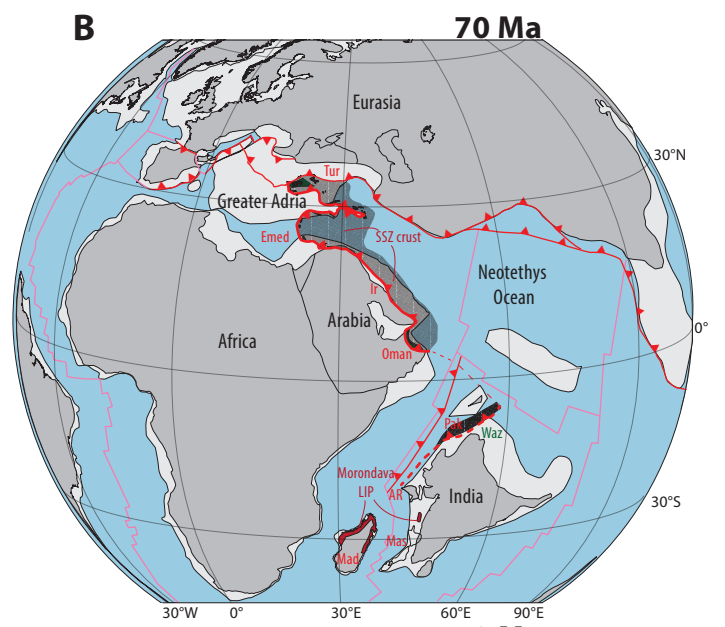
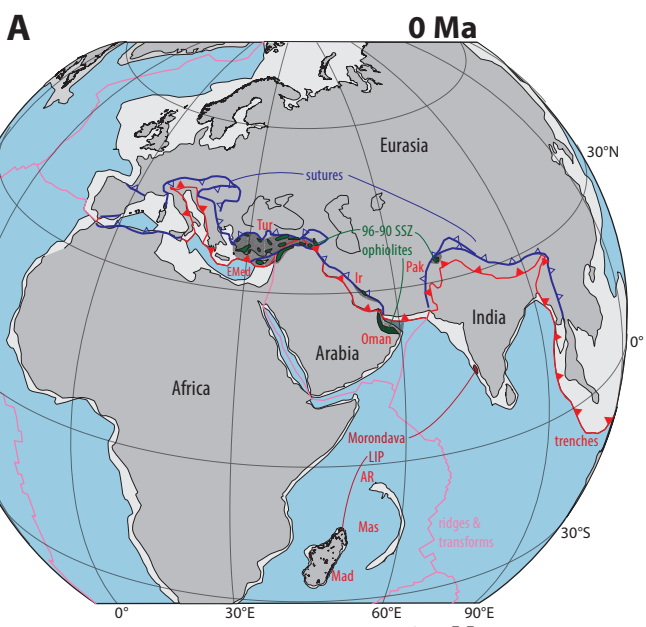
567 43 Kumar, P. *et al.* The rapid drift of the Indian tectonic plate. *Nature* **449**, 894-897, doi:10.1038/nature06214  
568 (2007).

569 44 Lamb, S. & Davis, P. Cenozoic climate change as a possible cause for the rise of the Andes. *Nature* **425**,  
570 792-797 (2003).

571 45 van der Meer, D. G., Spakman, W., van Hinsbergen, D. J. J., Amaru, M. L. & Torsvik, T. H. Towards  
572 absolute plate motions constrained by lower-mantle slab remnants. *Nature Geoscience* **3**, 36-40,  
573 doi:10.1038/ngeo708 (2010).

574 46 Tavani, S., Corradetti, A., Sabbatino, M., Seers, T. & Mazzoli, S. Geological record of the transition from  
575 induced to self-sustained subduction in the Oman Mountains. *Journal of Geodynamics* **133**, 101674 (2020).  
576 47 Tackley, P. J. Mantle convection and plate tectonics: Toward an integrated physical and chemical theory.  
577 *Science* **288**, 2002-2007 (2000).  
578 48 Coltice, N., Husson, L., Faccenna, C. & Arnould, M. What drives tectonic plates? *Science Advances* **5**,  
579 eaax4295 (2019).  
580 49 Dilek, Y. Ophiolite pulses, mantle plumes and orogeny. *Geological Society, London, Special Publications*  
581 **218**, 9-19 (2003).  
582 50 Ernst, R., Grosfils, E. & Mege, D. Giant dike swarms: Earth, venus, and mars. *Annual Review of Earth and*  
583 *Planetary Sciences* **29**, 489-534 (2001).  
584 51 Müller, R. D. *et al.* GPlates: building a virtual Earth through deep time. *Geochemistry, Geophysics,*  
585 *Geosystems* **19**, 2243-2261 (2018).  
586 52 Clube, T. M. M., Creer, K. M. & Robertson, A. H. F. Palaeorotation of the Troodos microplate, Cyprus.  
587 *Nature* **317**, 522, doi:10.1038/317522a0 (1985).  
588 53 Morris, A., Meyer, M., Anderson, M. W. & MacLeod, C. J. Clockwise rotation of the entire Oman  
589 ophiolite occurred in a suprasubduction zone setting. *Geology* **44**, 1055-1058 (2016).  
590 54 McQuarrie, N. & van Hinsbergen, D. J. J. Retrodeforming the Arabia-Eurasia collision zone: Age of  
591 collision versus magnitude of continental subduction. *Geology* **41**, 315-318, doi:10.1130/g33591.1 (2013).  
592 55 Monsef, I. *et al.* Evidence for an early-MORB to fore-arc evolution within the Zagros suture zone:  
593 Constraints from zircon U-Pb geochronology and geochemistry of the Neyriz ophiolite (South Iran).  
594 *Gondwana Research* **62**, 287-305 (2018).  
595 56 Galoyan, G. *et al.* Geology, geochemistry and <sup>40</sup>Ar/<sup>39</sup>Ar dating of Sevan ophiolites (Lesser Caucasus,  
596 Armenia): evidence for Jurassic Back-arc opening and hot spot event between the South Armenian Block  
597 and Eurasia. *Journal of Asian Earth Sciences* **34**, 135-153 (2009).  
598 57 Çelik, Ö. F. *et al.* Jurassic metabasic rocks in the Kızılırmak accretionary complex (Kargı region, Central  
599 Pontides, Northern Turkey). *Tectonophysics* **672-673**, 34-49, doi:10.1016/j.tecto.2016.01.043 (2016).  
600 58 Topuz, G. *et al.* Jurassic ophiolite formation and emplacement as backstop to a subduction-accretion  
601 complex in northeast Turkey, the Refahiye ophiolite, and relation to the Balkan ophiolites. *American*  
602 *Journal of Science* **313**, 1054-1087, doi:10.2475/10.2013.04 (2014).  
603 59 Ao, S. *et al.* U-Pb zircon ages, field geology and geochemistry of the Kermanshah ophiolite (Iran): From  
604 continental rifting at 79Ma to oceanic core complex at ca. 36Ma in the southern Neo-Tethys. *Gondwana*  
605 *Research* **31**, 305-318, doi:10.1016/j.gr.2015.01.014 (2016).  
606 60 Peters, T. & Mercolli, I. Extremely thin oceanic crust in the Proto-Indian Ocean: Evidence from the  
607 Masirah Ophiolite, Sultanate of Oman. *Journal of Geophysical Research: Solid Earth* **103**, 677-689,  
608 doi:10.1029/97jb02674 (1998).  
609 61 Gnos, E. *et al.* Bela oceanic lithosphere assemblage and its relation to the Reunion hotspot. *Terra Nova* **10**,  
610 90-95 (1998).  
611 62 Tapponnier, P., Mattauer, M., Proust, F. & Cassaigneau, C. Mesozoic ophiolites, sutures, and large-scale  
612 tectonic movements in Afghanistan. *Earth and Planetary Science Letters* **52**, 355-371 (1981).  
613 63 van Hinsbergen, D. J. J. *et al.* Greater India Basin hypothesis and a two-stage Cenozoic collision between  
614 India and Asia. *Proc Natl Acad Sci U S A* **109**, 7659-7664, doi:10.1073/pnas.1117262109 (2012).  
615 64 Yuan, J. *et al.* Rapid drift of the Tethyan Himalaya terrane before two-stage India-Asia collision. *National*  
616 *Science Review* (2020).  
617 65 Hébert, R. *et al.* The Indus-Yarlung Zangbo ophiolites from Nanga Parbat to Namche Barwa syntaxes,  
618 southern Tibet: First synthesis of petrology, geochemistry, and geochronology with incidences on  
619 geodynamic reconstructions of Neo-Tethys. *Gondwana Research* **22**, 377-397,  
620 doi:10.1016/j.gr.2011.10.013 (2012).  
621 66 Zahirovic, S. *et al.* Tectonic evolution and deep mantle structure of the eastern Tethys since the latest  
622 Jurassic. *Earth-Science Reviews* **162**, 293-337 (2016).  
623 67 Huang, W. *et al.* Lower Cretaceous Xigaze ophiolites formed in the Gangdese forearc: Evidence from  
624 paleomagnetism, sediment provenance, and stratigraphy. *Earth and Planetary Science Letters* **415**, 142-  
625 153, doi:10.1016/j.epsl.2015.01.032 (2015).  
626 68 Westerweel, J. *et al.* Burma Terrane part of the Trans-Tethyan arc during collision with India according to  
627 palaeomagnetic data. *Nature Geoscience* **12**, 863-868 (2019).  
628 69 Jagoutz, O., Royden, L., Holt, A. F. & Becker, T. W. Anomalously fast convergence of India and Eurasia  
629 caused by double subduction. *Nature Geoscience* **8**, 475-478, doi:10.1038/ngeo2418 (2015).

630 70 Höink, T. & Lenardic, A. Long wavelength convection, Poiseuille–Couette flow in the low-viscosity  
631 asthenosphere and the strength of plate margins. *Geophysical Journal International* **180**, 23-33 (2010).  
632 71 Höink, T., Jellinek, A. M. & Lenardic, A. Viscous coupling at the lithosphere-asthenosphere boundary.  
633 *Geochemistry, Geophysics, Geosystems* **12** (2011).  
634 72 Campbell, I. H. Testing the plume theory. *Chemical Geology* **241**, 153-176 (2007).  
635 73 Doubrovine, P. V., Steinberger, B. & Torsvik, T. H. A failure to reject: Testing the correlation between  
636 large igneous provinces and deep mantle structures with EDF statistics. *Geochemistry, Geophysics,*  
637 *Geosystems* **17**, 1130-1163 (2016).  
638 74 Steinberger, B. Topography caused by mantle density variations: observation-based estimates and models  
639 derived from tomography and lithosphere thickness. *Geophysical Journal International* **205**, 604-621  
640 (2016).  
641 75 Steinberger, B. & Becker, T. W. A comparison of lithospheric thickness models. *Tectonophysics* **746**, 325-  
642 338 (2018).  
643





Africa fixed

